Electronic Supplementary Material (ESI) for RSC Advances.

Supporting Information

Copolymers of Aniline and 2-aminoterephthalic Acid as a Novel Cathode Material for Hybrid Supercapacitor

Yi Gao,[a,+] Yu Li,[a,c,d,+] Haoran An,[a] Yiyu Feng,[a,c,d] and Wei Feng,[a,b,c,d*]

[a] School of Materials Science and Engineering, Tianjin University, Tianjin 300072, P. R China.

[b] Collaborative Innovation Centerof Chemical Science and Engineering (Tianjin), Tianjin 300072, P. R China.

[c] Key Laboratory of Advanced Ceramics and Machining Technology, Ministry of Education, Tianjin 300072, P. R China.

[d] Tianjin Key Laboratory of Composite and Functional Materials, Tianjin 300072, P. R China.

Corresponding Author： Dr. Wei Feng

***E-mail:** weifeng@tju.edu.cn

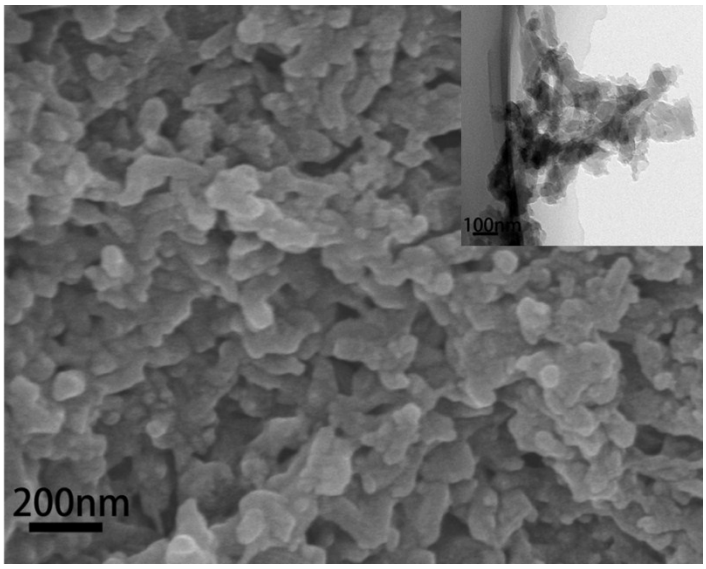

Fig. S1. The SEM image of PANI powder with the inset of the correspondent TEM image

Table S1. The electrical conductivities of copolymers and PANI

Component	P(ANI-*co*-ATA, 9:1)	P(ANI-*co*-ATA, 8:2)	P(ANI-*co*-ATA, 7:3)	P(ANI-*co*-ATA, 6:4)	PANI
Conductivity (S cm^{-1})	0.0972	0.135	0.0693	0.0412	0.0751

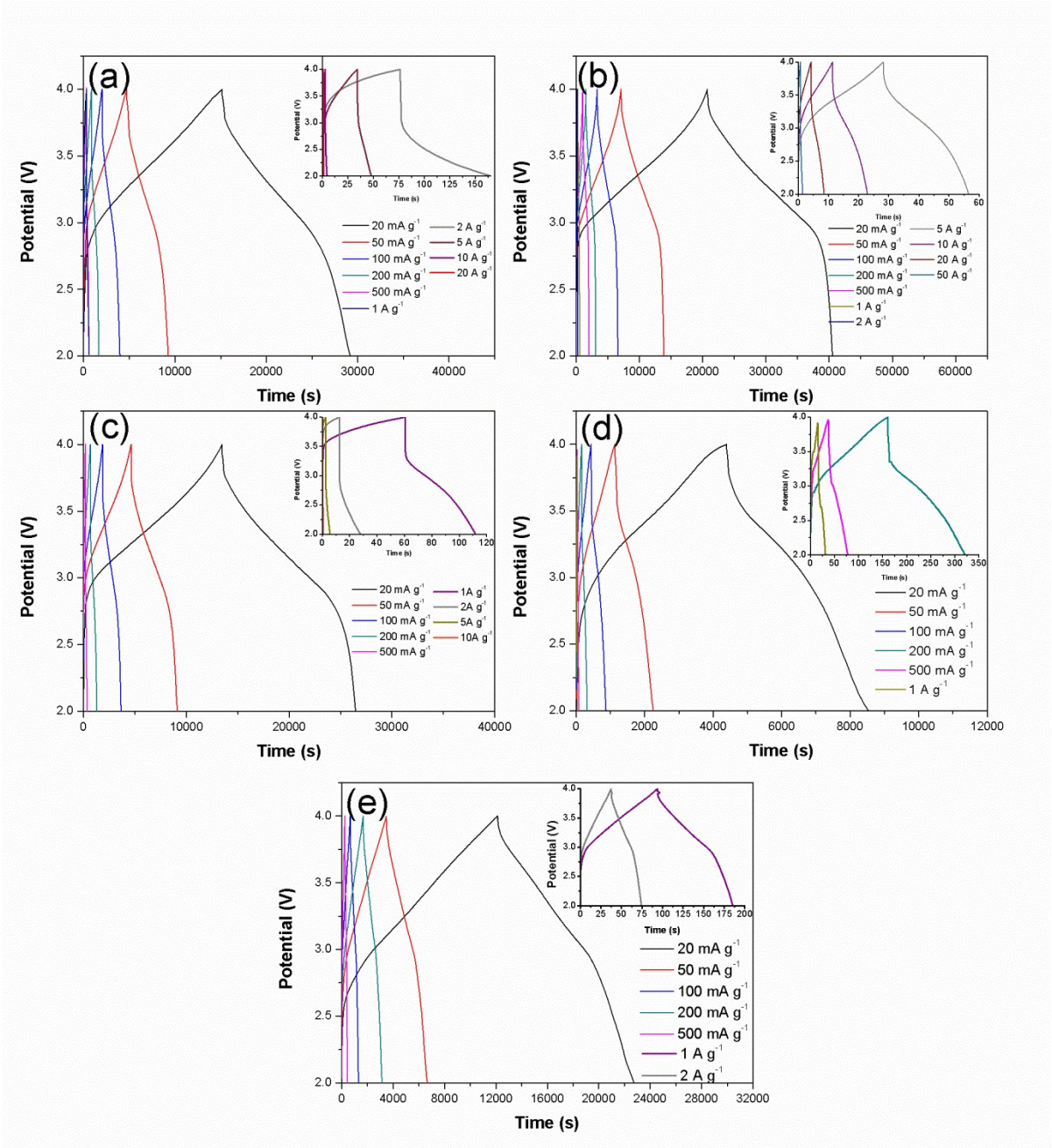

Fig. S2. Galvanostatic charge–discharge profiles of (a) P(ANI-*co*-ATA, 9:1), (b) P(ANI-*co*-ATA, 8:2), (c) P(ANI-*co*-ATA, 7:3), (d) P(ANI-*co*-ATA, 6:4) and (e) PANI electrodes at various current densities.

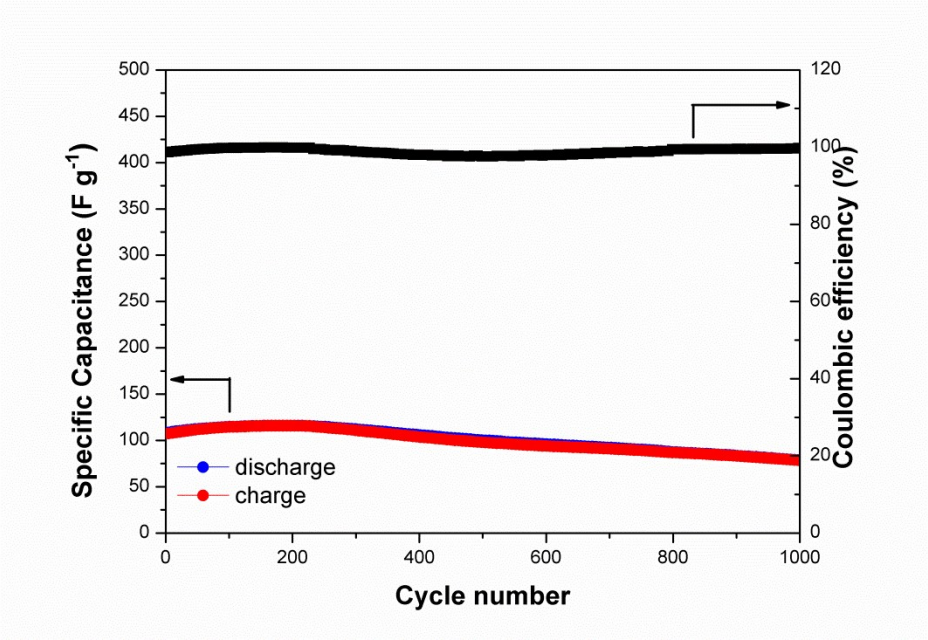

Fig. S3. The cycling stability of P(ANI-*co*-ATA, 8:2) at the current density of 2 A g^{-1} for 1000 cycles.

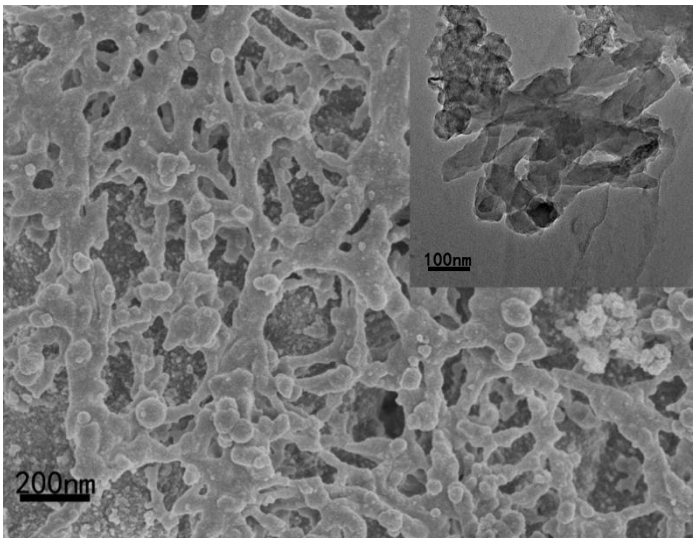

Fig. S4. The SEM image of P(ANI-*co*-ATA, 8:2) electrode after 1000 cycles at the current density of 2 A g^{-1} and the inset is the correspondent TEM image

Table S2. Electrochemistry testing condition of P(ANI-*co*-ATA,8:2) and other cathode materials which have been compared above.

Electrode material	Electrolyte	I_{max} (A g^{-1})	Voltage window (V)	Capacitor type	Capacity $_{max}$(I/mA g^{-1}) (F g^{-1})	Energy $_{max}$ (Wh kg^{-1})
P(ANI-*co*-ATA,8:2)	$LiClO_4$ （EC：DMC）	50	2-4	AC	198.1(20)	395.9
commercial AC [1]	$LiPF_6$ （EC：DMC）	0.65	2-4 1-5	AC	86(385) 114(385)	47.8 253.3
commercial AC [2]	$LiPF_6$ （EC：DMC）	0.12	3-4.6	AC	38.25(120)	13.6
activate graphene [3]	$LiPF_6$ （EC：DMC）	5.6	0-2.7	SC	182(1100)	184.3
TRGO [4]	$LiPF_6$ （EC：DMC）	0.1	3-4.6	AC	83.25(100)	29.6
NACs [5]	$LiPF_6$ （EC:DMC:DEC,10wt%FEC）	12.8	2-4.5	AC	189(400)	164.1
NPG [6]	$LiPF_6$ （EC:DMC:DEC,10wt%FEC）	10	2-4.5	AC	145.69(1000)	126.4
PNG [7]	$LiPF_6$ （EC：DMC）	10	0-2.7	SC	96(250)	97.2
Tube-like carbon [8]	$LiPF_6$ （EC：DMC）	2	0-3	SC	161(100)	201.3
3D porous graphene[9]	$LiPF_6$ （EC：DMC:DEC）	4	1.8-4.2	AC	168(100)	134.4
N-GMCS [10]	$LiPF_6$ （EC：DMC）	80	0-2.7	SC	87(100)	88.1

HNC [11]	$LiPF_6$ （EC：DMC:EMC）	2	3-4.5	AC	175.5(200)	54.8
AC [12]	$LiPF_6$ （EC：DEC）	0.025	2-4	AC	89.91(25)	49.9
3D-graphene [13]	$LiPF_6$ （EC：DMC:EMC）	2.5	2-4	AC	135(100)	75
3D graphene [14]	$LiPF_6$ （EC：DMC:EMC）	5	0-2.7	SC	187(50)	189.3
ODC [15]	$LiPF_6$ （EC：DMC）	10	3-4.6	AC	105(1000)	37.3
AC [16]	$LiPF_6$ （EC：DMC）	0.2	3-4.5	AC	148.5(200)	46.4
BTCA-derived carbon [17]	$LiPF_6$ （EC：DMC）	0.1	3-4.6	AC	166(100)	59.0
PHPNC [18]	$LiPF_6$ （EC：DMC）	3	2.5-4.5	AC	144(100)	80

AC：asymmetric capacitor SC: symmetric capacitor

Table S3. Values of the equivalent circuit components used for fitting the experimental curve.

Component	Fitted values		
	R_s / Ω	R_{ct} / Ω	$CPE \times 10^{-5}$ / F
P(ANI-*co*-ATA, 9:1)	3.66	95.42	1.87
P(ANI-*co*-ATA, 8:2)	3.14	85.13	2.16
P(ANI-*co*-ATA, 7:3)	3.72	250.91	5.21
P(ANI-*co*-ATA, 6:4)	3.44	185.36	3.08
PANI	3.57	191.43	4.73

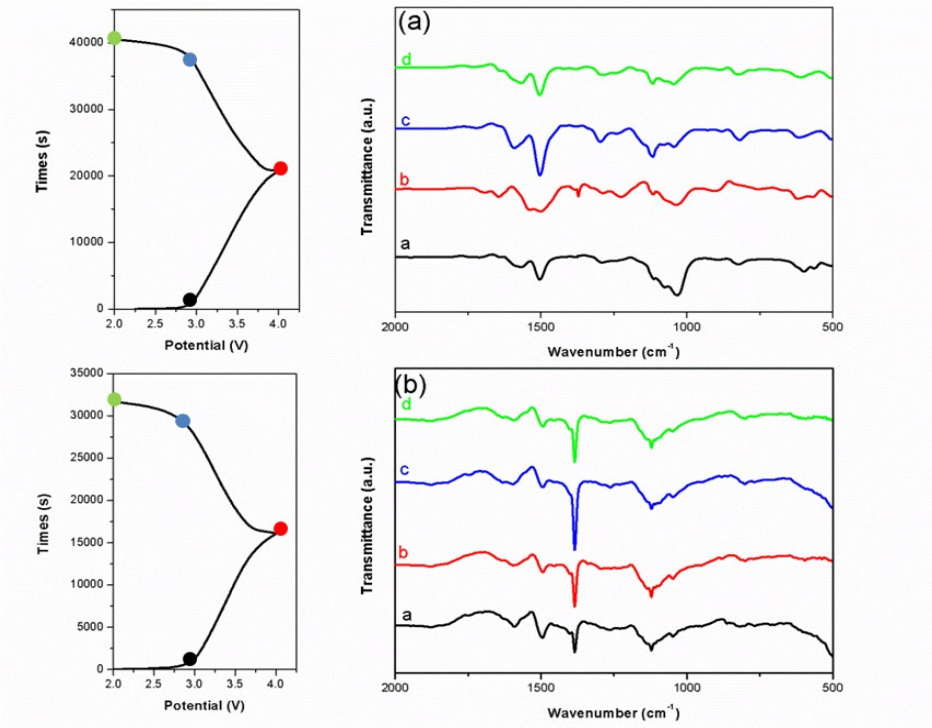

Fig. S5. Ex-situ FT-IR spectra of the P(ANI-co-ATA, 8:2) electrode in the first (a) and one hundredth (b) cycle, taken at different states as marked by A, B, C, D in the left corresponding charge-discharge profile. The FT-IR spectra of P(ANI-*co*-ATA, 8:2) electrode at different states in the first cycles are similar to that of pristine P(ANI-*co*-ATA, 8:2) powder. The peaks at 1096 cm^{-1} imply the existence of ClO_4^-. Besides, the varied intensity ratio of I_{1570} and I_{1500} during the charge-discharge process, demonstrates the standard p-type doping/dedoping mechanism. The FT-IR spectra of P(ANI-co-ATA, 8:2) electrode in the one hundredth cycles, at different states, are reminiscent of that for as-made electrode. The peaks lied at 1700, 1250 cm^{-1}, which are assigned to C=O and C-O stretching vibration of carboxylic groups respectively, and the peaks locate at 1570, 1500 cm^{-1}, which are attributed to the C=C stretching of the quinoid and benzenoid rings , demonstrate the structural stability of P(ANI-co-ATA, 8:2) electrode during the cycling process. Additionally, the ClO_4^-

doping/dedoping energy storage mechanism is also verified by the changed intensity ratio of I_{1570} and I_{1500} and existant peak located at 1096 cm^{-1}.

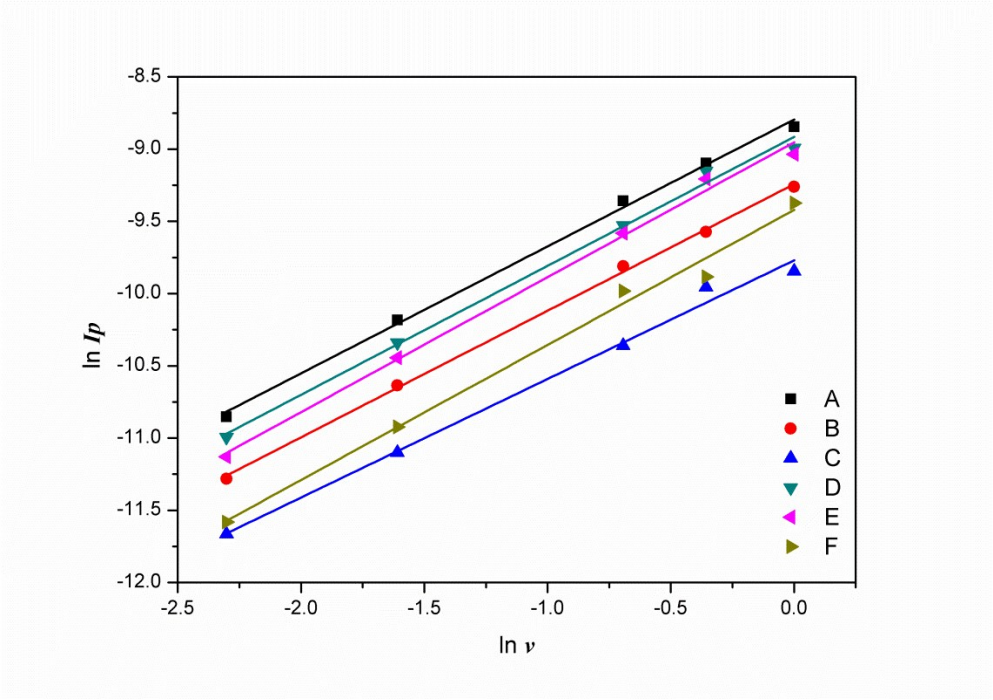

Fig. S6. The fitted lines of ln *Ip versus* In *v* for separating the diffusion controlled and capacitive controlled electrochemical reaction of P(ANI-*co*-ATA, 8:2) electrode. The capacitive contribution is calculated by using the equations as following:

$$I_p = a v^b$$

$$\ln I_p = \ln a + b \ln v$$

In which I_p is the peak current (A), v is the scan rate (mV s^{-1}), a and b are constants. When the b-value is close to 1, the electrochemical reaction is mainly controlled by capacitance; while the b-value approaches to 0.5, the anion diffusion controlled process becomes dominant. The current densities of different redox peaks at various scan rates could be read from CV curves (Fig. 4c) and hence In *Ip* and corresponding ln *v* could be simulated by using Eq. S2 so as to obtain the b-value by the slope of the fitted line. The b-value for redox peaks in CV curves shown in Fig. S6 are listed in Table S1. It can be find that all slopes are close to 1, indicating the approximate linear

relation between I_p and v and the capacitive-controlled process for all peaks. [19] Moreover, the current density in CV curve is consisted by two parts, which are capacitive effect (k_1v) and diffusion- controlled reaction ($k_2v^{1/2}$). Because of the fixed k_1 and k_2 in the same electrochemical reaction, the peak current of the same voltage position at different scan rates to calculate the k_1 and k_2 using the equation as the following:

$$i = k_1v + k_2v^{1/2}$$

The capacitive contribution is depicted in Fig. 4d.

Table S4. The slopes of each fitting lines

Peak number	A	B	C	D	E	F
Slope	0.8785	0.8763	0.8208	0.89249	0.9340	0.9348

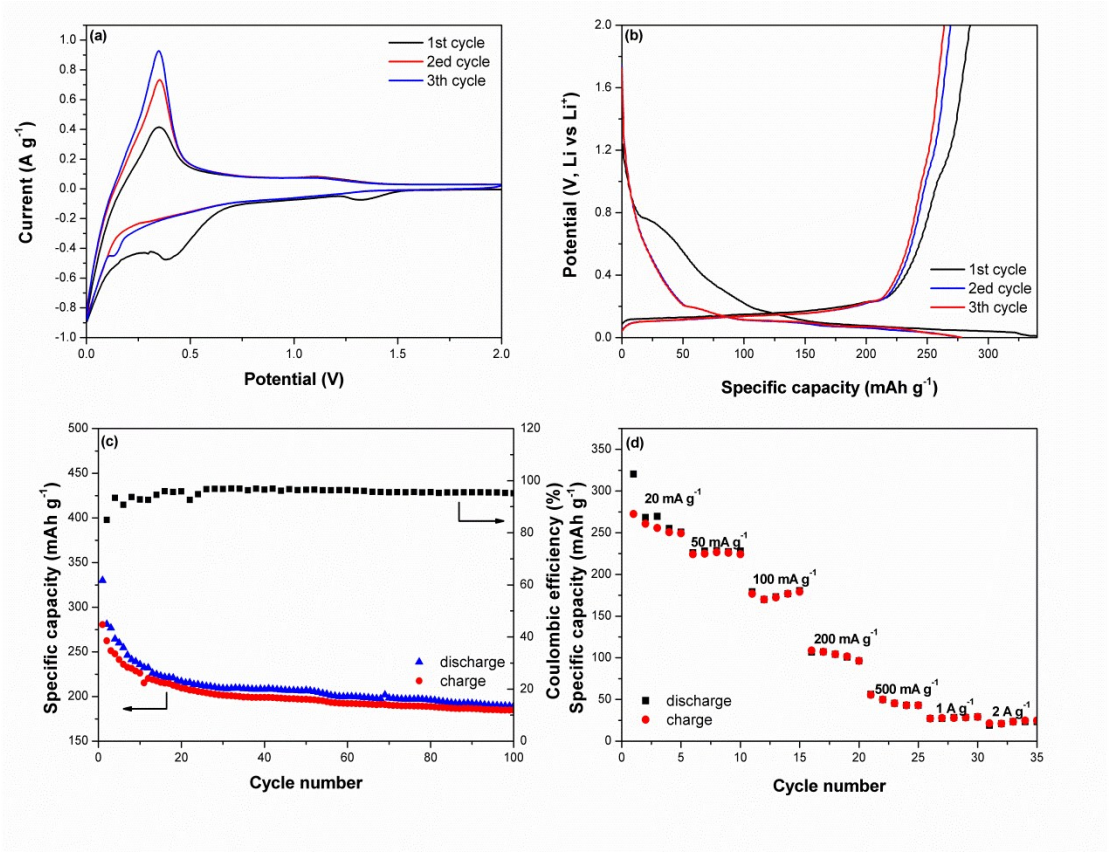

Fig. S7. Electrochemical performance of the MCMB electrode: (a) CV curves at a scan rate of 0.5 mV s^{-1}, (b) Galvanostatic charge-discharge profiles at a current density of 20 mA g^{-1}, (c) Cycling performance at the current density of 20 mA g^{-1}, (d) Rate capability at different current densities.

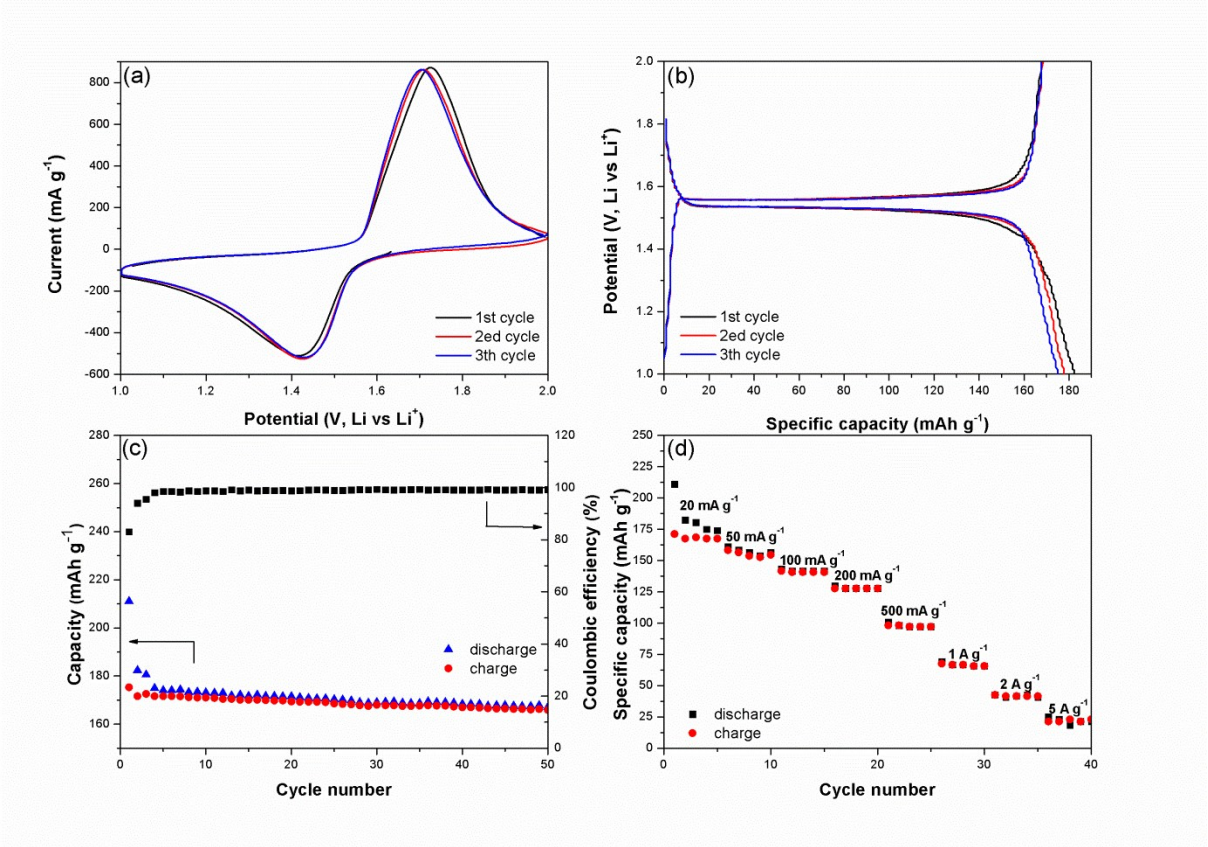

Fig. S8. Electrochemical performance of the LTO electrode: (a) CV curves at a scan rate of 0.5 mV s^{-1}, (b) Galvanostatic charge-discharge profiles at a current density of 20 mA g^{-1}, (c) Cycling performance at the current density of 20 mA g^{-1}, (d) Rate capability at different current densities.

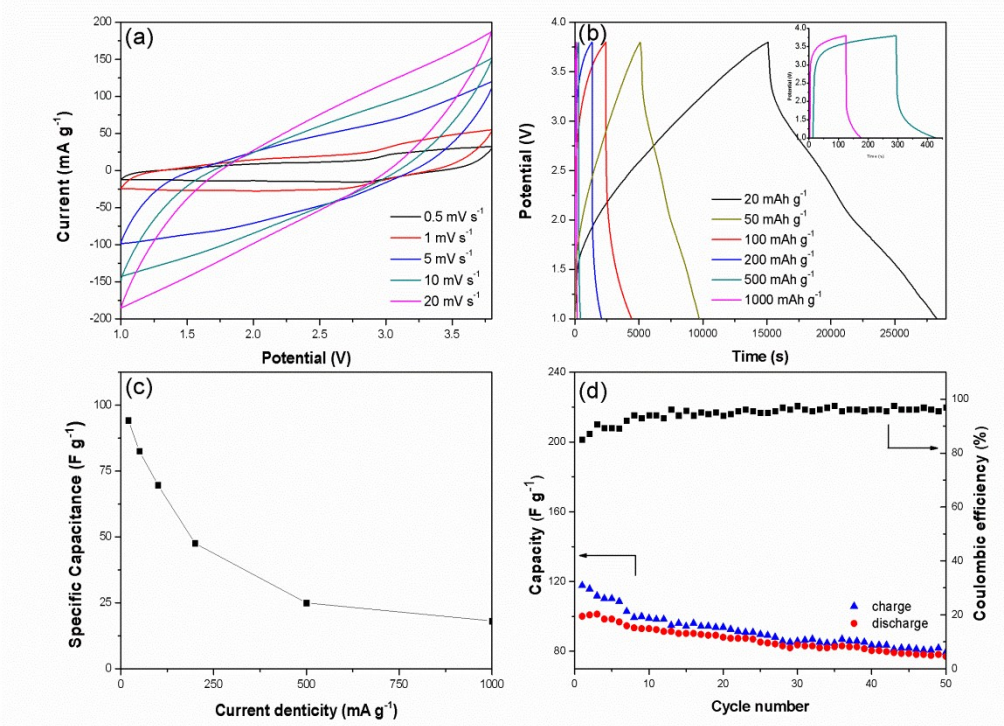

Fig. S9. Electrochemical performance of P(ANI-*co*-ATA, 8:2)//MCMBs HSC: (a) The CV curves of the P(ANI-*co*-ATA, 8:2)//MCMBs HSC is slightly deviated from that of P(ANI-*co*-ATA, 8:2) at the same scan rate due to the synergetic effect of two different energy storage mechanism. However, the shape of CV curves is drastically deformed with the increase of scan rate, which is caused by the poor rate capability of MCMBs anode; (b) The charge-discharge profiles of P(ANI-*co*-ATA, 8:2)//MCMBs HSC at different current densities. The doping/dedoping energy storage characteristic is still observed at the current density as low as 20 mA g^{-1}, but the charge-discharge profiles turn to liner slopes at the current density higher than 50 mA g^{-1} due to the ineffective Li^+ insertion/extraction into/from the interlayer of MCMBs at relatively high loads; (c) The rate capability of the P(ANI-*co*-ATA, 8:2)//MCMBs HSC, whose specific capacitance values are 94.3, 82.6, 69.7, 47.6, 25 and 18.1 F g^{-1}, based on the total mass of both electrode materials, at the current densities of 20, 50, 100, 200, 500,

1000 mA g^{-1}, respectively. (d)The cycling performances of P(ANI-*co*-ATA, 8:2)//MCMBs HSC tested at the current density of 20 mA g^{-1}, which shows a stable cycling performance over 50 cycles with the capacitance retention of 77% and the Coulombic efficiency above 90% after the cycling test.

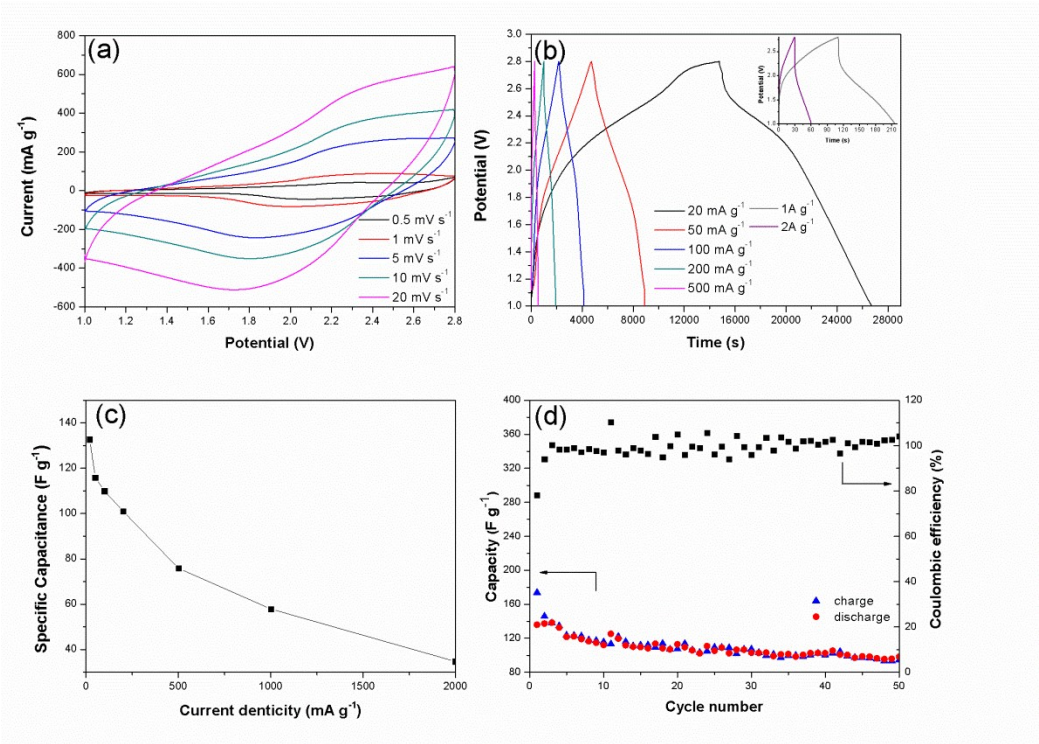

Fig. S10. Electrochemical performance of P(ANI-co-ATA, 8:2)//$Li_4Ti_5O_{12}$: (a) Cyclic voltammetry curves at various scan rates from 0.5 mV s^{-1} to 20 mV s^{-1}. The asymmetric CV curves of the P(ANI-co-ATA, 8:2)//LTO HSC at various scan rates stem from the combination of fast intercalation reaction at the anode and the rapid anions transport at the cathode. (b) Galvanostatic charge/discharge curves at serious of current densities; (c) Rate capability at different current densities. The charging/discharging profiles, recorded at current densities from 0.02 to 2 A g^{-1} based on the total active mass of cathode and anode materials, of the P(ANI-co-ATA, 8:2)//LIB HSC exhibit the similar shape with that of copolymer cathode, and the specific capacitance values of the HSC are 132.7, 115.9, 110.1, 101.6, 75.9, 57.9, 34.7 F g^{-1}at the current densities of 20, 50, 100, 200, 500, 1000 ,2000 mA g^{-1} respectively. The P(ANI-co-ATA, 8:2)//$Li_4Ti_5O_{12}$ HSC exhibits stable cycling performance without significant capacitance fading, with the capacitance retention of 72%, after 50

cycles at the current density of 20 mA g^{-1}.

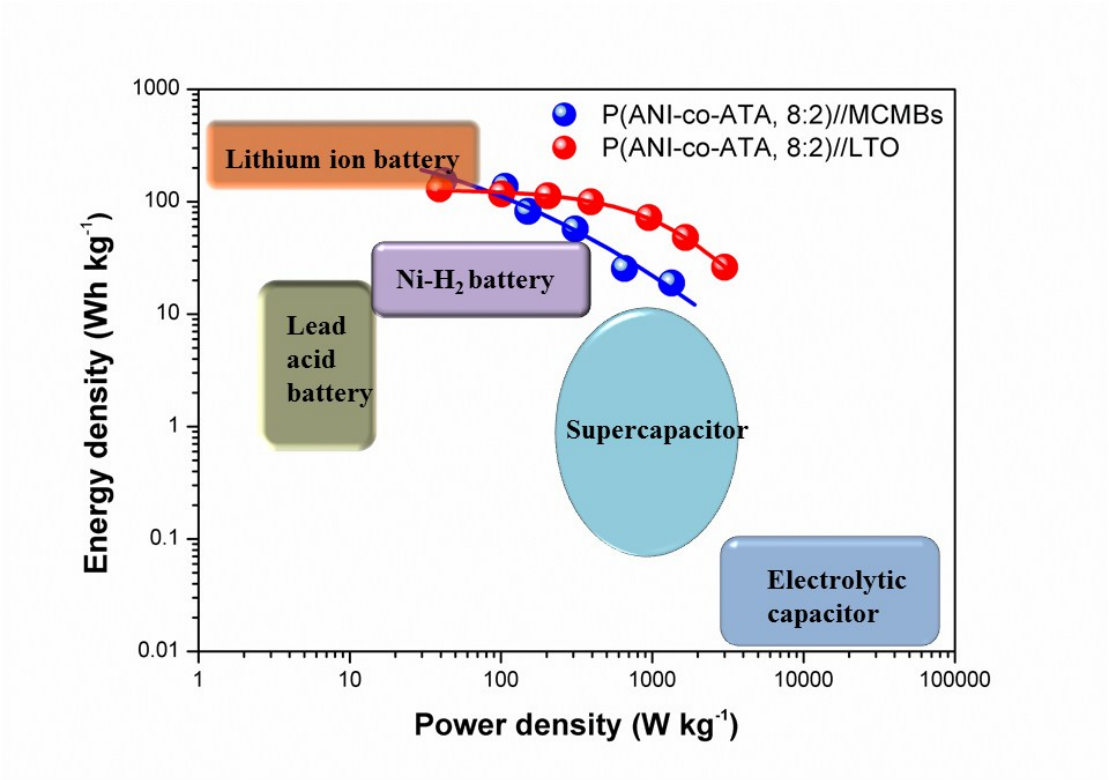

Fig. S11. Ragone plots of the P(ANI-*co*-ATA, 8:2)//MCMB and P(ANI-*co*-ATA, 8:2)//LTO compared with commercial energy storage device.

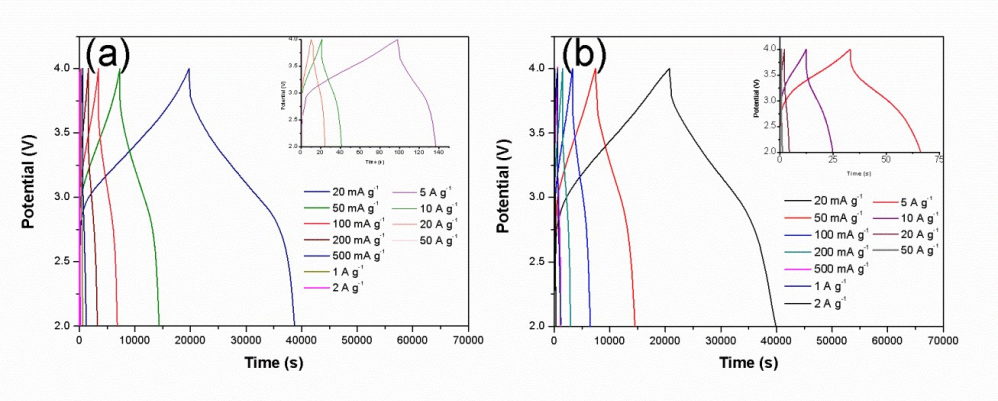

Fig. S12. The Galvanostatic charge–discharge profiles of P(ANI-co-ATA, 8:2) in the parallel tests

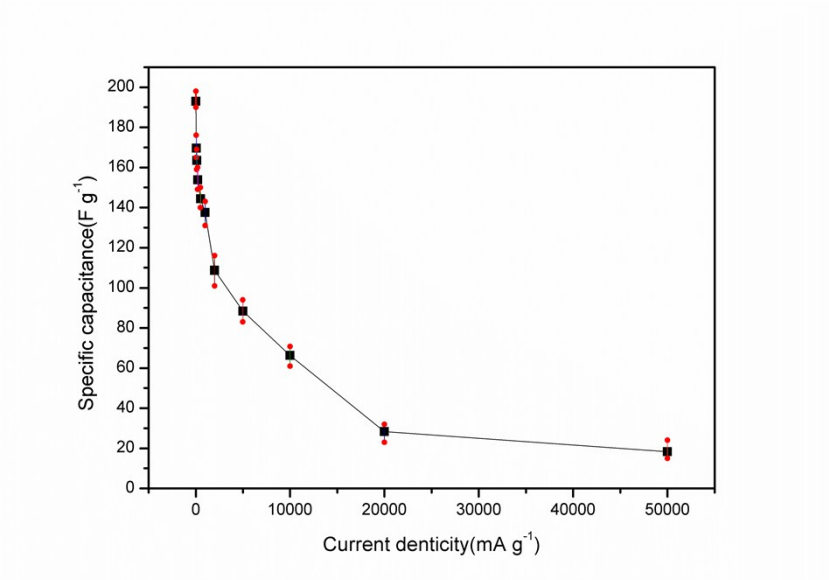

Fig. S13. The specific capacitances of P(ANI-co-ATA, 8:2) electrodes versus current densities with error bar. The short error bars indicate the excellent reproducibility of the material.

Notes and references

1 V. Khomenko, E. Raymundo-Piñero,; F. Béguin, J. Power Sources, 2008, 177, 643-651.
2 V. Aravindan,; W. Chuiling,; M. V. Reddy, G. S. Rao, B. V. R. Chowdari, S. Madhavi, Phys. Chem. Chem. Phys., 2012, 14, 5808-5814.
3 M. D. Stoller, S. Murali, N. Quarles, Y. Zhu, J. R. Potts X. Zhu, R. S. Ruoff, Phys. Chem. Chem. Phys., 2012, 14, 3388–3391.
4 V. Aravindan, D. Mhamane, W. C. Ling, S. Ogale, S. Madhavi, ChemSusChem, 2013, 6, 2240-2244.
5 B. Li,; F. Dai, Q. Xiao, L. Yang, J. Shen, C. Zhang, M. Cai, Energ. Environ. Sci., 2016, 9, 102-106.
6 F. Zhang, Y. Tang, H. Liu, H. Ji, C. Jiang, J. Zhang, C. S. Lee, ACS Appl Mater Inter, 2016, 8, 4691-4699.
7 L. Ye, Q. Liang, Y. Lei, X. Yu, C. Han, W. Shen, Q. H. Yang, J. Power Sources, 2015, 282, 174-178.
8 P. Sennu, H. J. Choi, S. G. Baek, V. Aravindan, Y. S. Lee, Carbon 98 （2016）58-66.
9 T. Zhang, F. Zhang, L. Zhang, Y. Lu, Y. Zhang, X. Yang, Y. Huang, Carbon, 2015, 92, 106-118.
10 X. Yu,; C. Zhan, R. Lv, Y. Bai, Y. Lin, Z. H. Huang， F. Kang, Nano Energy, 2015, 15, 43-53.
11 M. Yang, Y. Zhong, J. Ren, X. Zhou,; J. Wei,; Z. Zhou, Adv. Energy Mater., 5, 2015, 1500550.
12 J. Zhang, Z. Shi, C. Wang, Electrochim. Acta, 2014, 125, 22-28.
13 K. Leng, F. Zhang, L. Zhang, T. Zhang, Y. Wu, Y. Lu, Y. Chen, Nano. Res., 2013, 6, 581-592.
14 F. Zhang, T. Zhang, X. Yang, L. Zhang, K. Leng, Y. Huang, Y. Chen, Energ. Environ. Sci., 2013, 6, 1623-1632.
15 R. Gokhale, V. Aravindan, P. Yadav, S. Jain, D. Phase, S. Madhavi, S. Ogale, Carbon, 2014, 80, 462-471.
16 H. Kim, M. Y. Cho, M. H.Kim, K. Y. Park, H. Gwon, Y. Lee, K. Kang, Adv. Energy Mater., 2013, 3, 1500-1506.
17 D. Mhamane, V. Aravindan, M. S. Kim, H. K. Kim, K. C. Roh, D. Ruan, K. B. Kim, J. Mater. Chem. A, 2016, 4, 5578-5591.
18 H. Wang, Y. Zhang, H. Ang, Y. Zhang, H. T. Tan, Y. Zhang, H. J. Fan, Adv. Funct. Mater., 2016, 26, 3082-3093.
19 Z. Jian, V. Raju, Z. Li, Z. Xing, Y. S. Hu,; X. Ji, Adv. Funct. Mater., 2015, 25, 5778-5785.